Taylor & Francis
Taylor & Francis Group

Stratigraphic and Petrophysical assessment of ASL sandstone reservoir in northern and central October Field, Gulf of Suez

Kareem Bakr[a], Tharwat Abdel-Fattah[b], Mohamed Shaaban[b], Ahmed Diab [ID][b], Hany Helmi[c] and Hossam M. El-Sayed [ID][d]

[a]Geomechanics Department, Gulf of Suez Petroleum Company (GUPCO), Cairo, Egypt; [b]Geology Department, Faculty of Science, Alexandria University, Alexandria, Egypt; [c]Petroleum Consultant, Subsurface, Cairo, Egypt; [d]Marine Environment Division, Marine Geophysics Laboratory, National Institute of Oceanography and Fisheries, NIOF, Cairo, Egypt

ABSTRACT

This study analysed the depositional environment and diagenesis of the ASL Member reservoir in the October oil field located in the Gulf of Suez Basin, Egypt. Sedimentological and petrophysical techniques were used to interpret data from four wells: OCT-J7B, GS173-2, GS184-4A, and GS195-3, penetrating various rock types, including sandstone, carbonate, and fractured basement reservoirs. Log correlations of OCT-J7B and GS173-2 showed they penetrated pre-Miocene strata, while GS184-4A and GS195-3 reached the Rudeis section. Based on seismic-based structural maps, all wells except GS173-2 were drilled down-dip of the main Clysmic fault. The Hawara shale and the older shales in the Rudeis section were found to be the reservoir's lateral seal, and the Lagia shale was found to be its vertical seal. Core analysis of OCT-J7B revealed the ASL as limestone interbedded with shale and sandstone deposited in a proximal submarine fan lobe, while GS184-4A and GS195-3 were located in amid-fan carbonate system. The comparisons of core and log data from the four wells yielded excellent matches, and the iso-parametric mapping delineated reservoir quality horizontally and hydrocarbon potentiality. The study recommends sitting future wells away from uplifts and suggests further reservoir characterization and evaluation of potential zones in the ASL Member.

1. Introduction

Egypt's most prolific and prospective oil province is the Gulf of Suez, with commercial-scale oil production starting in 1909. It is an intracontinental, late Oligocene rifted basin initially formed during the early Paleozoic as a narrow embayment of the Tethys (Jarrige et al. 1990; Bosworth et al. 1998; Montenat et al. 1998; Abdel Fattah et al. 2020; Diab and Khalil 2021). The Gulf of Suez basin contains over 80 oil field reservoirs ranging in age from Precambrian to Quaternary age rocks. The study area is within October Field, located in the north-central part of the Gulf of Suez. It is bounded by latitudes 28°49′40″ N and 29°01′00″ N and longitudes 32°57′33″ and 33°10′00″ E (Figure 1).

October Field is Egypt's third largest oil field, discovered in 1977 with the drilling of GS195–1. It was followed by drilling the Nubian offset producers GS195–2, GS185–1, and GS196-2A wells. In 1979, GS173–2 was spudded as a Nubia exploratory well to test the Nubia and Nukhul drilling results. In 1981, the OCT-D2 development well

was drilled to establish production from the GS172 block. In 1989, ASL reservoir sandstone was discovered on the hanging wall of the main fault bounding October Field (Zahran 1986; Abdine et al. 1992; Lelek et al. 1992). Among many drilled wells scattered in the study area, four wells were given by Egyptian General Petroleum Corporation (EGPC) to elucidate the hydrocarbon potentiality of the Early-middle Miocene ASL Member of Rudeis Formation in the downthrown side.

The scope of work of the study area was to provide a better and more detailed description of the subsurface stratigraphic and geologic setting, as well as a detailed petrographic evaluation and depositional setting of the ASL sandstone reservoir in the north-central part of the main October Field. Data and materials were provided by EGPC through the Gulf of Suez Petroleum Company, including seismic data, wireline logs, ditch samples for the selected intervals in ASL sandstone, thin sections from core samples, and core photos in the studied wells (Abdel-Fattah et al. 2019; El-Dakak et al. 2021). This study addressed an

Figure 1. Location map of the October Field and available wells.

integration between sedimentological and petrophysical techniques applied to ASL Member as one of the main producing rock units in the Early-Middle Miocene age in October Field. The techniques enabled us to interpret the depositional environment of this reservoir, investigate the diagenetic processes that enhanced and reduced its reservoir quality and determine the petrophysical parameters and their lateral variation to show the best net-to-gross pay locations.
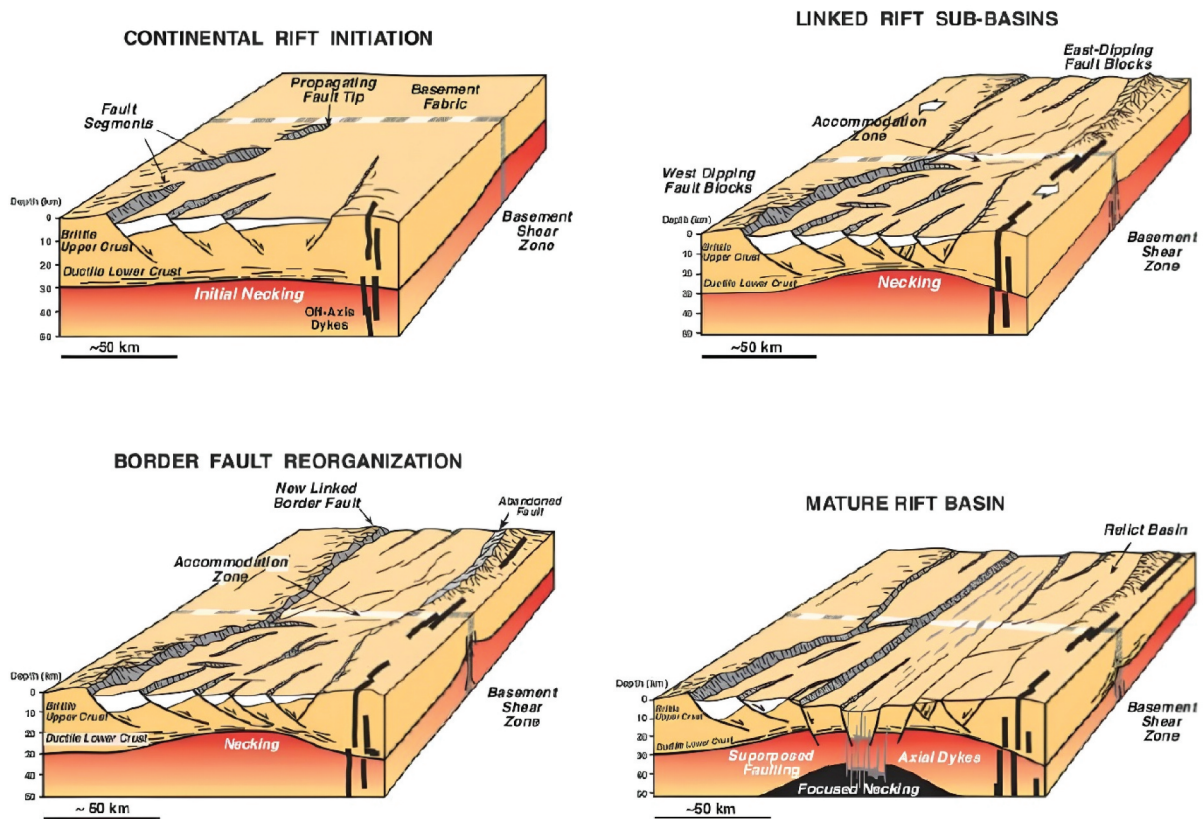
Figure 2. Synoptic models for the evolution of the Gulf of Suez - Red Sea rift system (Bosworth 1994).

2. Geological setting

2.1. Structural framework of the Gulf of Suez

The Tectonic Evolution and Structural Framework of the Gulf of Suez, Egypt occupies the northeastern portion of the African plate, which experienced convergence with the Eurasian plate to the North and divergence with the Arabian plate to the East. This led to approximately N-S convergent movement between the African and Eurasian plates. As a result, the Syrian Arc fold system formed along the northeastern part of Egypt during the Late Cretaceous to Early Tertiary time, and the Suez rift was initiated due to the N60E extension before the Early Miocene time (Robson 1971; Garfunkel and Bartov 1977; Lyberis 1988; Patton et al. 1994; Younes and McClay 2002). The tectonostratigraphic events are shown in Figure 2 and include the onset of rifting during the Late Oligocene to Early Miocene (Chattian-Aquitanian). This rift stage is evidenced by the deposition of marine sediments in the lower part of the Nukhul Formation in the south and the rapid transition from the Abu Zenima red beds to the shallow marine facies.

Increasing amounts of evaporite were recorded during the deposition of the Rudeis Formation (Burdigalian-Early Langhian) and Belayim Formation (Late Serravallian). As a result, the Gulf of Suez has been divided into three central tectonic provinces: Galala, Belayim, and Morgan. The Galala-Abu Zenima Accommodation zone and the Morgan Accommodation zones indicate a change in the half-graben polarities in the rift basin, where rift border faults are affected by the pre-existing basement structures. Southwesterly dipping strata and northeasterly antithetic dipping faults characterise the northern Araba\Darag Dip Province. The Belayim Central Dip Province has shallow pre-Miocene structures underlying the Miocene sediments, and the Amal-Zeit Southern Dip Province has been subjected to severe erosion (Bosworth and McClay 2001).

2.2. Stratigraphic framework of the Gulf of Suez

The stratigraphic record of the Suez rift basin can be divided into five distinct tectonic megasequences, which are from older to younger: 1) Paleozoic passive margin, 2) Mesozoic rift to passive margin, 3) Syrian Arc inversion, 4) late Oligocene to middle Miocene rift, and 5) late Miocene to recent rift (Figure 3) (Peijs et al. 2012; Temraz and Dypvik 2017). Megasequence 1 (Paleozoic from Cambrian to Permian) comprises Precambrian gneisses, volcanic, and metasediments deformed and metamorphosed during the Pan African orogeny terminated about 550 Ma (Stern 1981, 1994; Kröner 1984, 1993; Stoeser
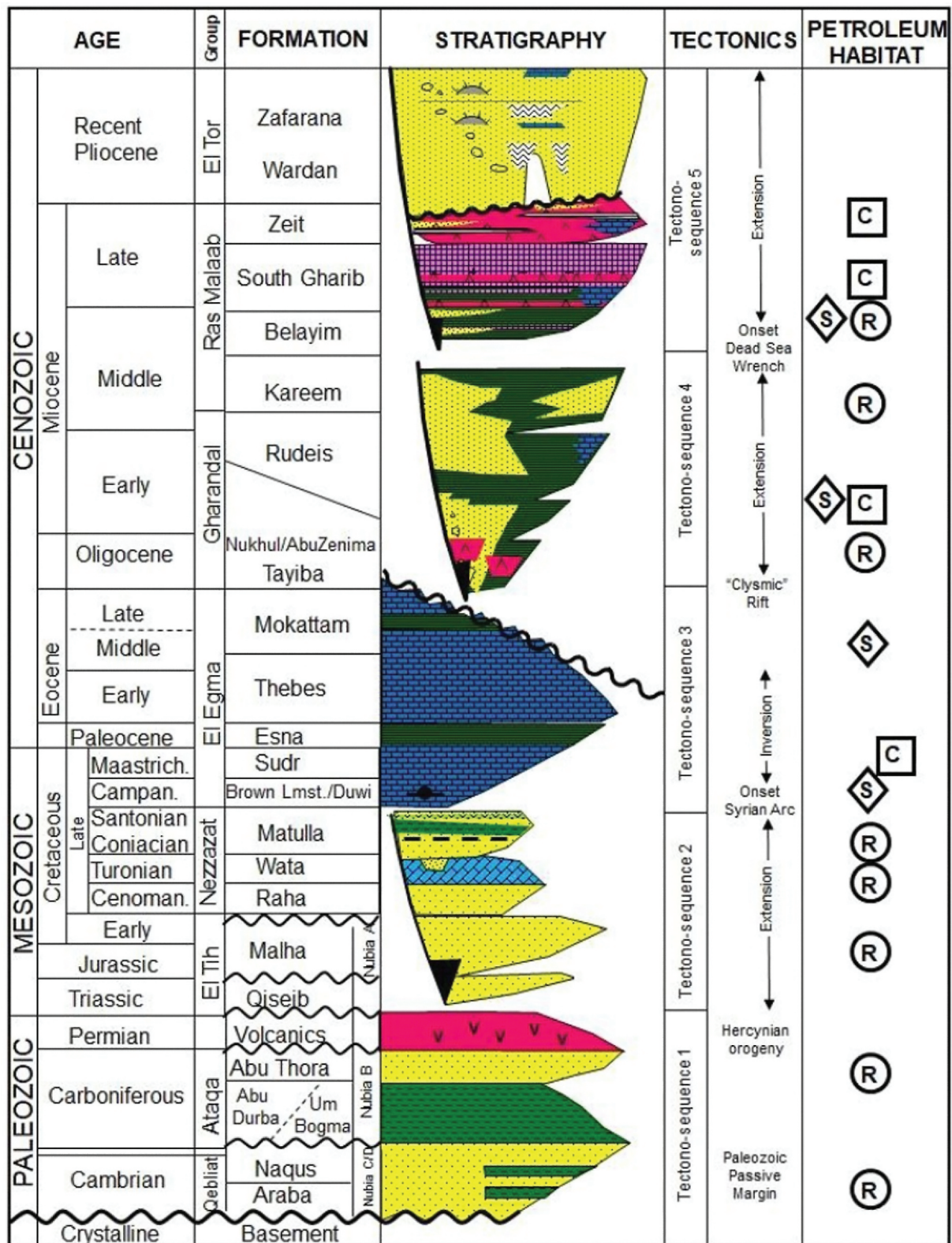
Figure 3. Tectonostratigraphic section for the gulf of Suez (Peijs et al. 2012).

and Camp 1985). The Basement rocks of the Gulf of Suez exhibit some strong pre-rift structural fabrics that have influenced the late Cenozoic rifting structural trends (Younes et al. 1998). The Paleozoic Nubia, also known as the megasequence 2 (Jurassic to Coniacian) sediments, are present in Egypt and were deposited in a broad passive margin setting during the opening of the Neo-Tethys Ocean. The marine Jurassic sediments are known from outcrops south of Ain Sokhna, wells in the Darag basin, and the Jurassic half graben bounding faults later inverted by the Santonian "Syrian Arc" event (Bevan and Moustafa 2012).

Megasequence 3 (Santonian to Late Eocene) was associated with folding, faulting, and uplifting, resulting in a uniform white chalk bed
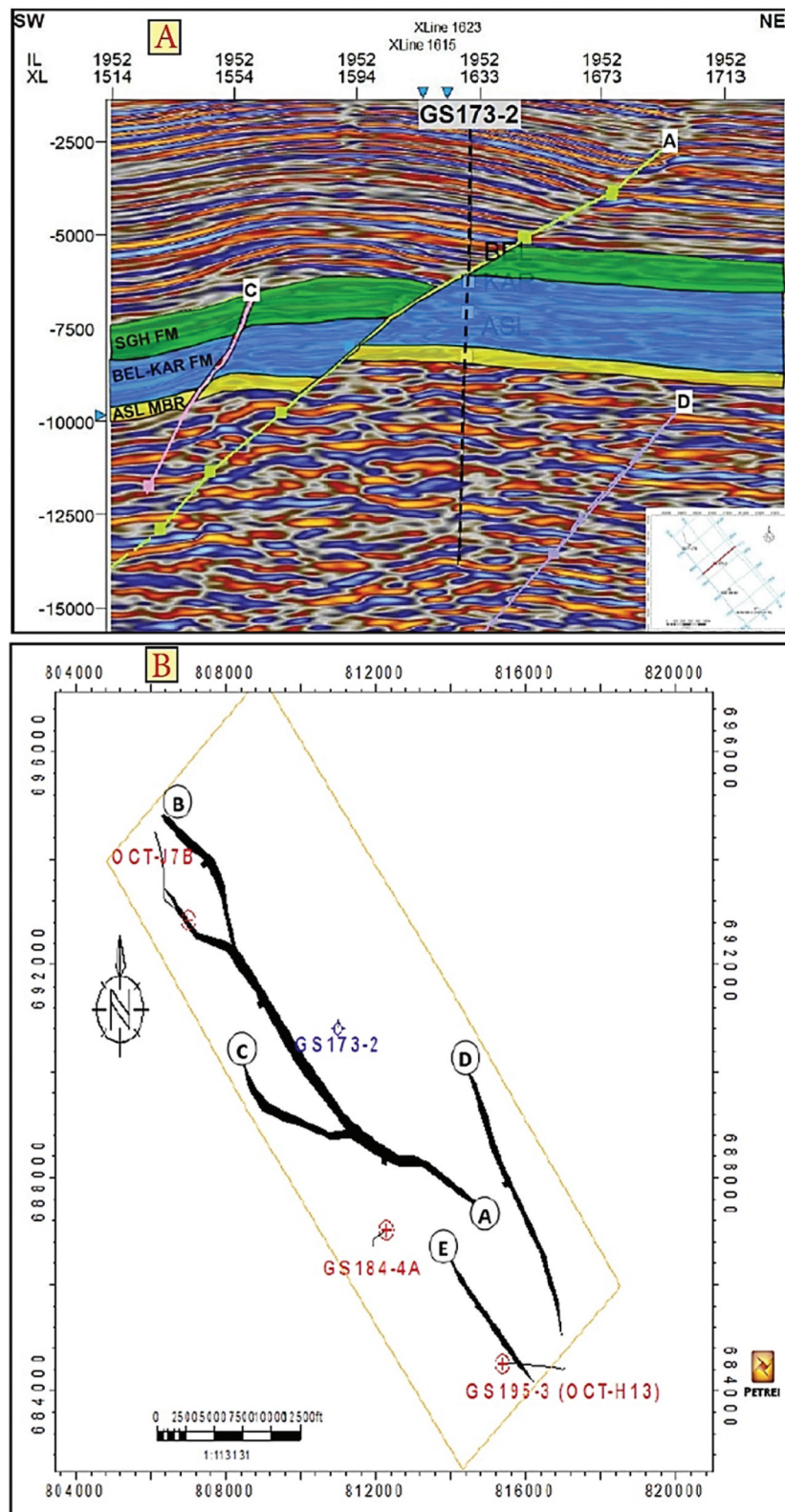
Figure 4. A) interpreted seismic section shows three faults and the three interpreted seismic horizons. B) fault polygons for the top ASL member in the study area.

deposition. The Syrian arc affected this megasequence as it has an angular unconformity between Campanian Brown Limestone Formation and Matulla Formation, while the Megasequence 4 (Latest Oligocene to Middle Miocene "Rift Phase") defines the active rifting phase of the Suez Rift, characterised by basaltic dikes, sills, and flows along the margins and in the subsurface data set of the rift as an indication of rift initiation (Said, 1990a and b; Moustafa and Khalil 1995; Peijs et al. 2012). The early Syn-rift tectonic strata associated with these dikes are the Abu Zenima and Nukhul Formations and the early Miocene age.
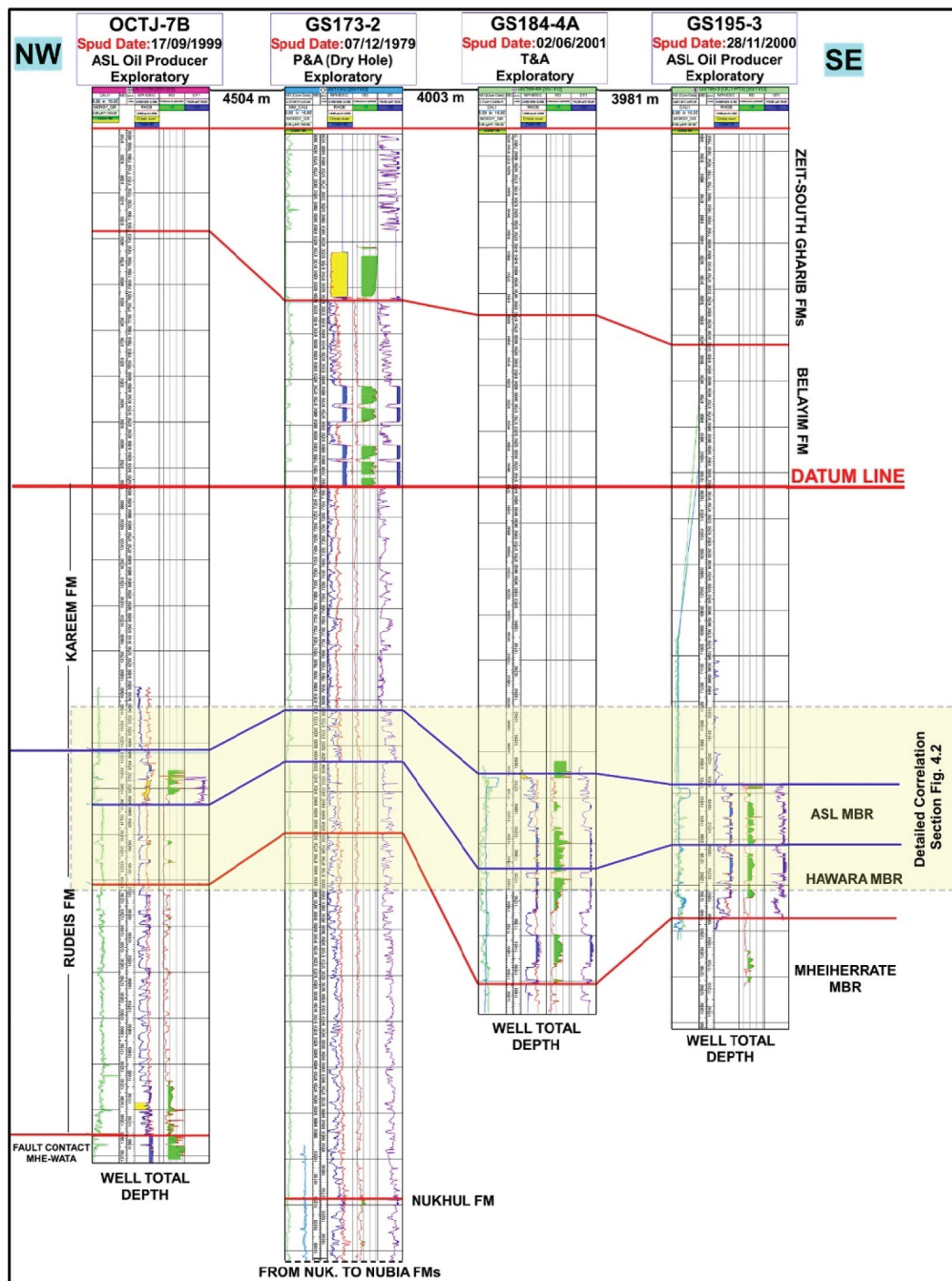
Figure 5. Stratigraphic correlation among wells in the study area for the entire drilled stratigraphic section.

The syn-rift sedimentary sequence is subdivided into four main formations: the Nukhul, lower Rudeis, Upper Rudeis, and Kareem Formations. The biostratigraphic data suggest deposition in marginal marine to shelf environments, with little direct palaeontological evidence for deep water deposition. The Upper Rudeis Formation (Langhian) was deposited as a submarine fan system in the North Darag, October, and South Belayim subbasins, with a gross interval isopach greater than 2000 ft. (600 m) and thin isopach values of 164 ft. (50 m) and 650–1300 ft. (200–400 m). It was also thinner than the Lower Rudeis in all sub-basins due to the presence of point sources, such as the quartz-rich Wadi Feiran source. In addition, Wadi Wardan/Wadi Baba acted as an entry point source to the Lagia sub-basin during this time, resulting in a mixture of calcareous and siliceous sediments. Paleo-bathymetric interpretations suggest the similarity of Lower Rudeis and Upper Rudeis sediments be deposited in outer neritic to bathyal water depths, except for some proximal environments landward of the coastal faults. The thickest anhydrite in the Lagia and October sub-basins is 100–150 ft. (30–45 m) of clean, massive anhydrite bodies, while Lagia anhydrite
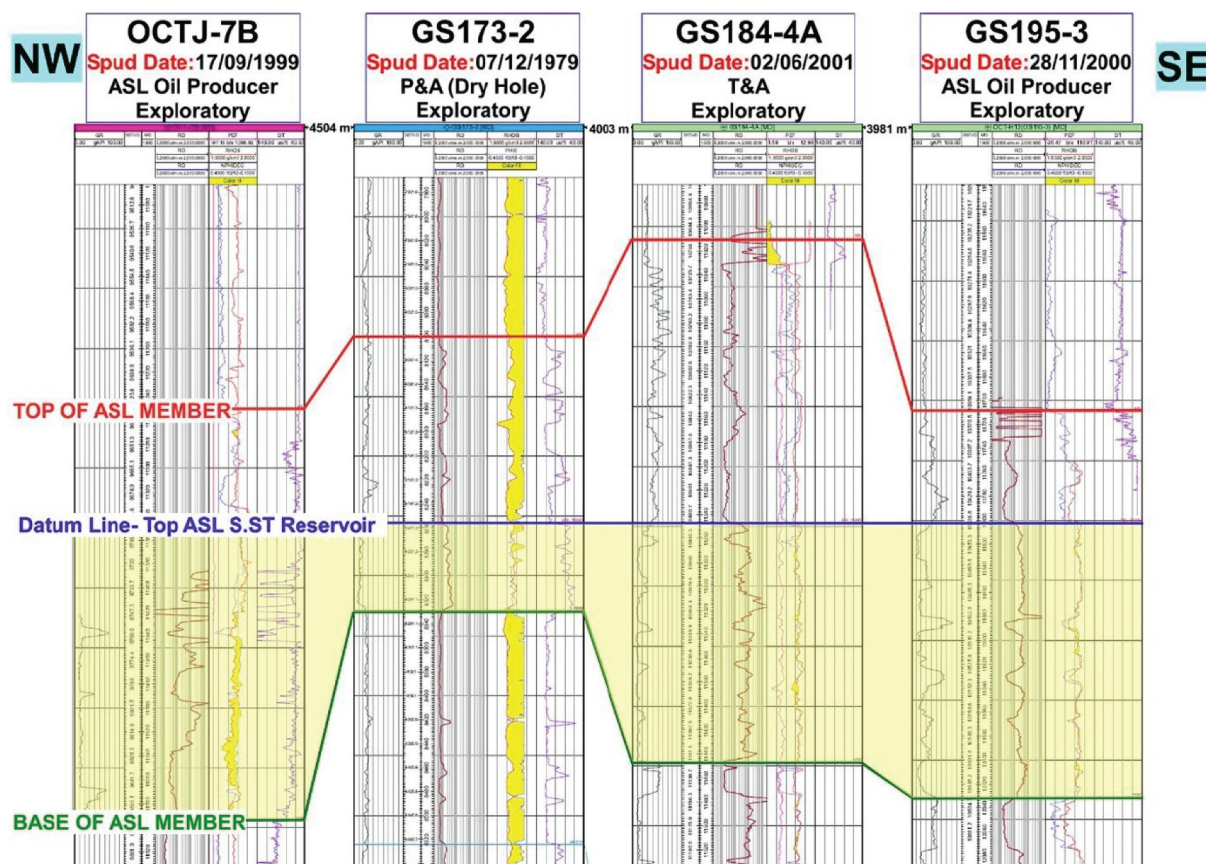
Figure 6. Stratigraphic correlation showing variation in ASL member sandstone thickness.

is absent to extremely thin in the North Darag basin. The Kareem Formation gross isopach and net sand thickness maps show that October, July, and Ramadan fields were clearly in place structurally, as sands onlap these impressive footwall structures.

Megasequence 5 (Late Miocene to Recent) is the onset of the Dead Sea/Levant transform boundary, approximately 14 Ma (Serravallian). It is distinct from the Oligo-Miocene rifting phase in both areas and is confined to the major linked coastal fault system, which has an extension direction of NNE – SSW to N – S (Peijs et al. 2012). The subsidence history in the October area shows a dramatic increase in the subsidence rate from approximately 10 Ma. The primary evaporite deposition was due to marine basin evaporation during the Serravallian and continued into the Pliocene.

2.3. Stratigraphy and hydrocarbon habitat of October Field

October Field primarily produces oil from the sandstones of the Cretaceous Nubia and the localised sandstones and localised dolomites of the Cenomanian-Senonian Nezzazat Group. The Nubia Formation consists of stacked massive sandstones interbedded with massive to thin lenticular shales and has a maximum thickness of 2800 ft., with an average thickness of 2300 ft. in the Main Field Area (Lelek et al. 1992; Aly et al.

2015). The Cenomanian transitional Nubia contains ~ 25% of the Nubia reserves and is a laterally continuous 115–200 ft. thick interval of marginal marine, thinly interbedded, calcareous sandstones and shales. The Nezzazat Group has an average thickness of 1200 ft. and comprises the Matulla, Wata, Abu Qada, and Raha Formations. The main reservoirs are thinly laminated, coastal plain and shoreline sandstone units in the Matulla Formation, meandering fluvial channel sandstones in the Wata Formation, and marine calcareous locally glauconitic sandstones near the base of the Raha Formation. Also, the Miocene ASL Member consists of 230–320 ft. of sandy limestone and sandstone within Upper Rudeis shales and represents a potential reservoir. The principal source rocks for the oil in the North October and October Fields are carbonates of the Upper Cretaceous Campanian Brown Limestone (the lower unit of the Sudr Formation or Duwi Formation). Thicknesses in the Gulf of Suez are 80–230 ft., and TOC content is ~ 1–5%, up to 8% regionally, and averages 2.6% (Lelek et al. 1992).

Stone (1992) studied the reservoir potential of the ASL Member in north October Field, concluding that three sandstone intervals at the base of the reservoir are responsible for 91% of the oil production and reservoir porosity and permeability range from 17% to 27% and 30 millidarcy's to 3 darcies, respectively. Davies and Bliefnick (2001) studied sedimentology and depositional setting of the lower Miocene ASL
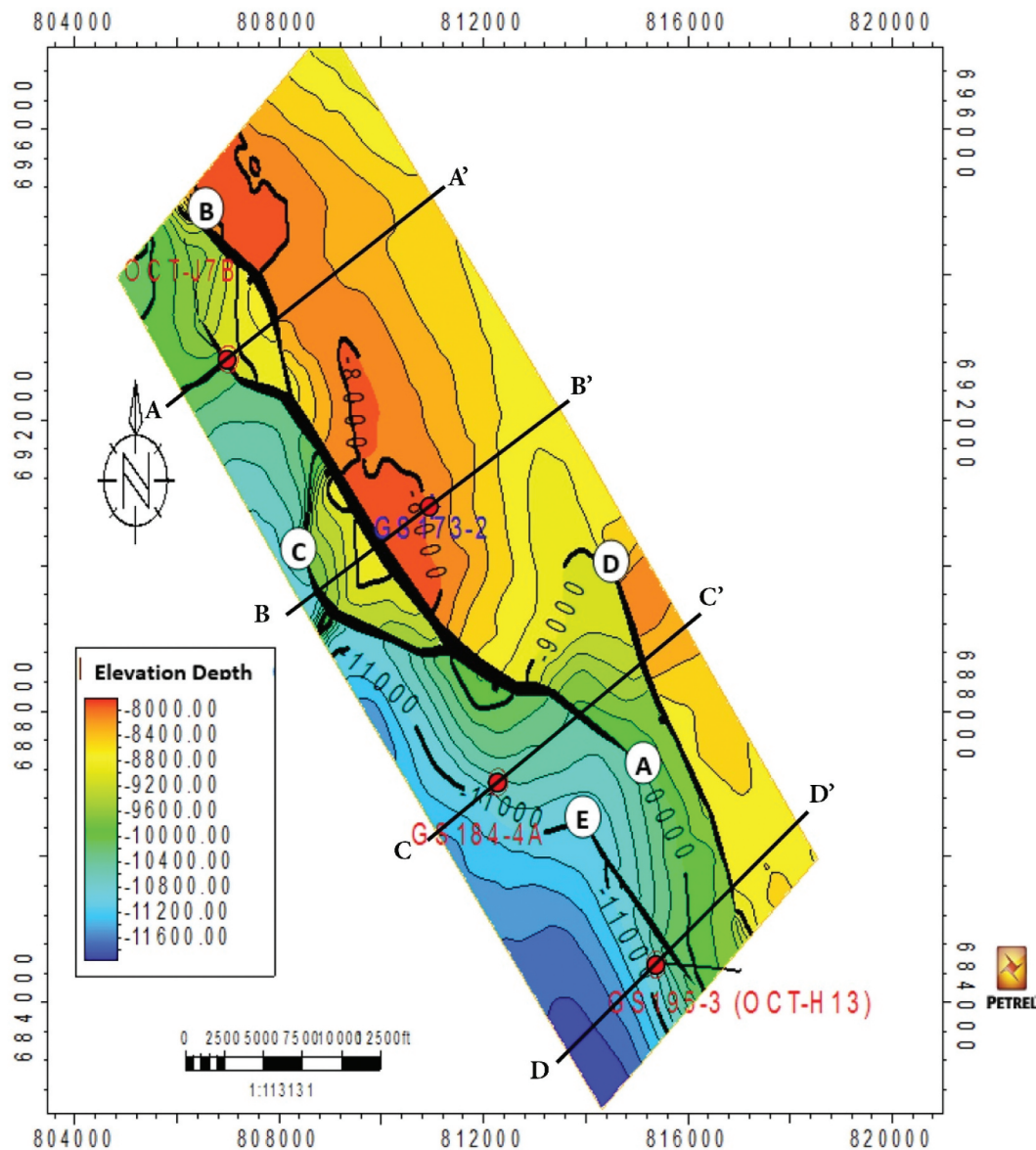
Figure 7. Depth structure contour map for the top of ASL member showing the geologic cross sections illustrated in Figure 8.

and Hawara Members, concluding that the cored intervals are dominated by two principal lithofacies: carbonate-rich packstones/grainstones and medium-grained quartz-rich sandstones. El Ghamri et al. (2002) and El-Shahat et al. (2009) studied hydrocarbon generation and charging in the October Field, concluding that gravity flows are the dominant depositional process. Finally, Lashin et al. (2011) evaluated ASL and Hawara formations using seismic and log-derived properties, revealing good oil-bearing potentiality.

3. Methodology

3.1. Seismic interpretation

The October Field 3D survey was shot in 1992 by GEOTEAM EXPLORATION, processed by C.G. Company in 1993, and reprocessed by Western Atlas Company. The main target of the seismic interpretation

is to create a complete structure framework and one or more horizon depth maps throughout the imaged area (Liner 2004; Mercaroni 2014). Interpretations of the data can be improved by comparing marker beds or other correlation points picked on well logs with significant reflections on the seismic section.

3.2. Stratigraphic correlation and petrophysical evaluation

Stratigraphic correlation is a process of comparing one log with another of the same type to obtain more information than can be derived from the log alone. This study used four wells to evaluate the hydrocarbon potentiality of the ASL reservoir in the study area. The open-hole log data were collected and digitised, including the traditional tools such as shallow and deep resistivity, neutron, density, sonic, and gamma-ray logs. The cross-plot technique was used to show the lithological and
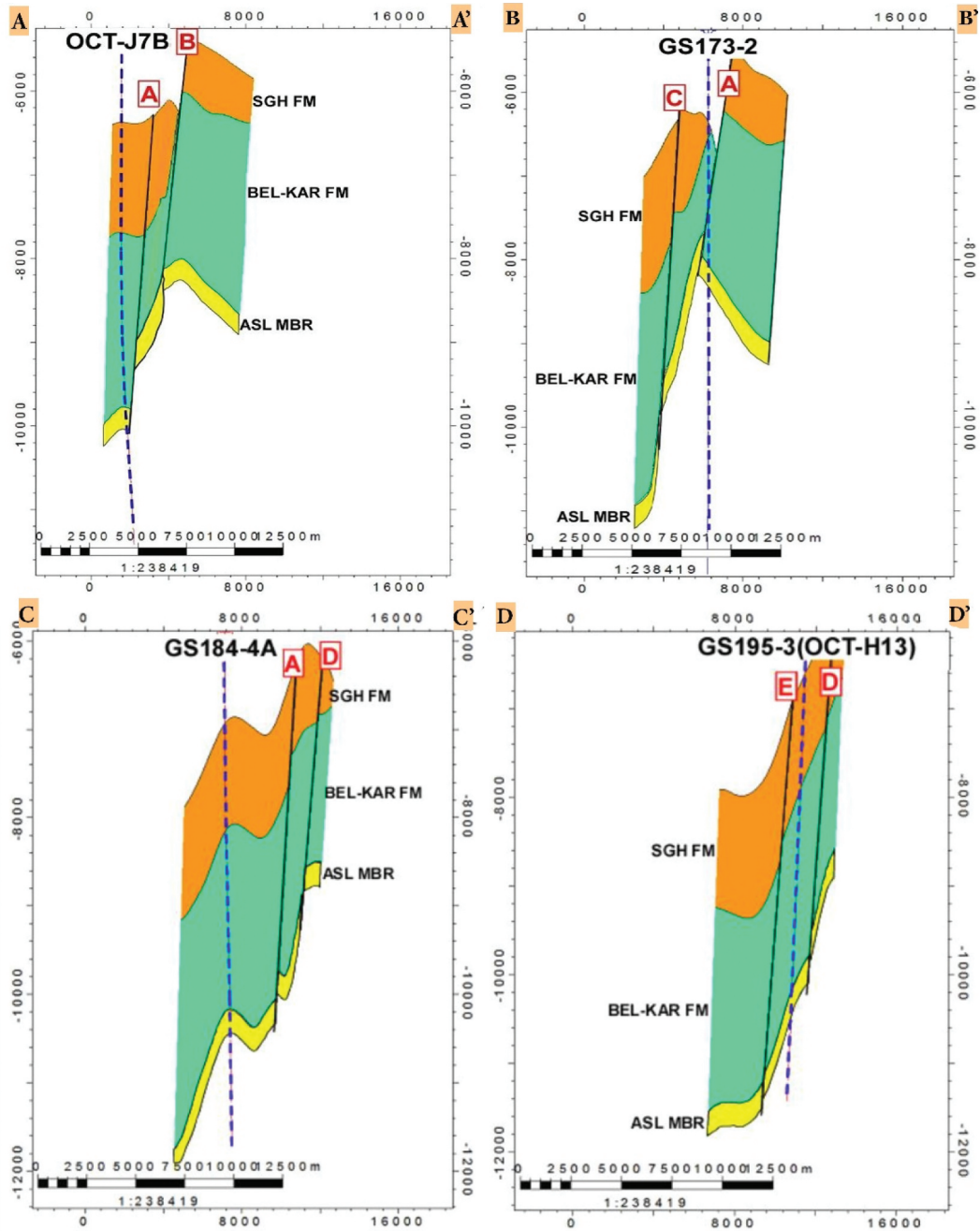
Figure 8. Geologic cross sections (A-A') NE-SW dip cross section across OCT-J7B well, (B-B') NE-SW dip cross section across GS173–2 well, (C-C') NE-SW dip cross section across GS184-4A well, and (D-D') NE-SW dip cross section across GS195–3 well.

mineralogical components of the reservoir, and the obtained ASL Member reservoir properties were mapped to investigate their lateral variation and distribution all over the October oil Field study area.

The well log data were interpreted to transform the downhole measurements into physical rock parameters including shale volume, permeability, porosity, water saturation, and hydrocarbon saturation. We estimated the shale content (V_{sh}) for ancient rocks from the GR-log using Larinov's equation (1), and the outcomes validated from Neutron-Density logs.

$$V_{sh} = 0.33 * \left[2^{(2*I_{GR})} - 1 \right] \qquad (1)$$

$$I_{GR} = \frac{\left(GR_{log} - GR_{min} \right)}{\left(GR_{max} - GR_{min} \right)} \qquad (2)$$

Where:

I_{GR} is the gamma − ray index;
GR_{log} is the reading of the GR curve in the reservoir Formation; GR_{min} is the minumum reading of the GR curve in front of clean sand; GR_{max} is the maximum reading of the GR curve at shale lithology

We used the equation (3) of Tiab and Donaldson (2015) to calculate the neutron porosity ($_{Ncorr}$) and equations (4) of Wyllie et al. (1958) to derive the porosity from the bulk density log (ρ_b), then the porosity value was averaged.
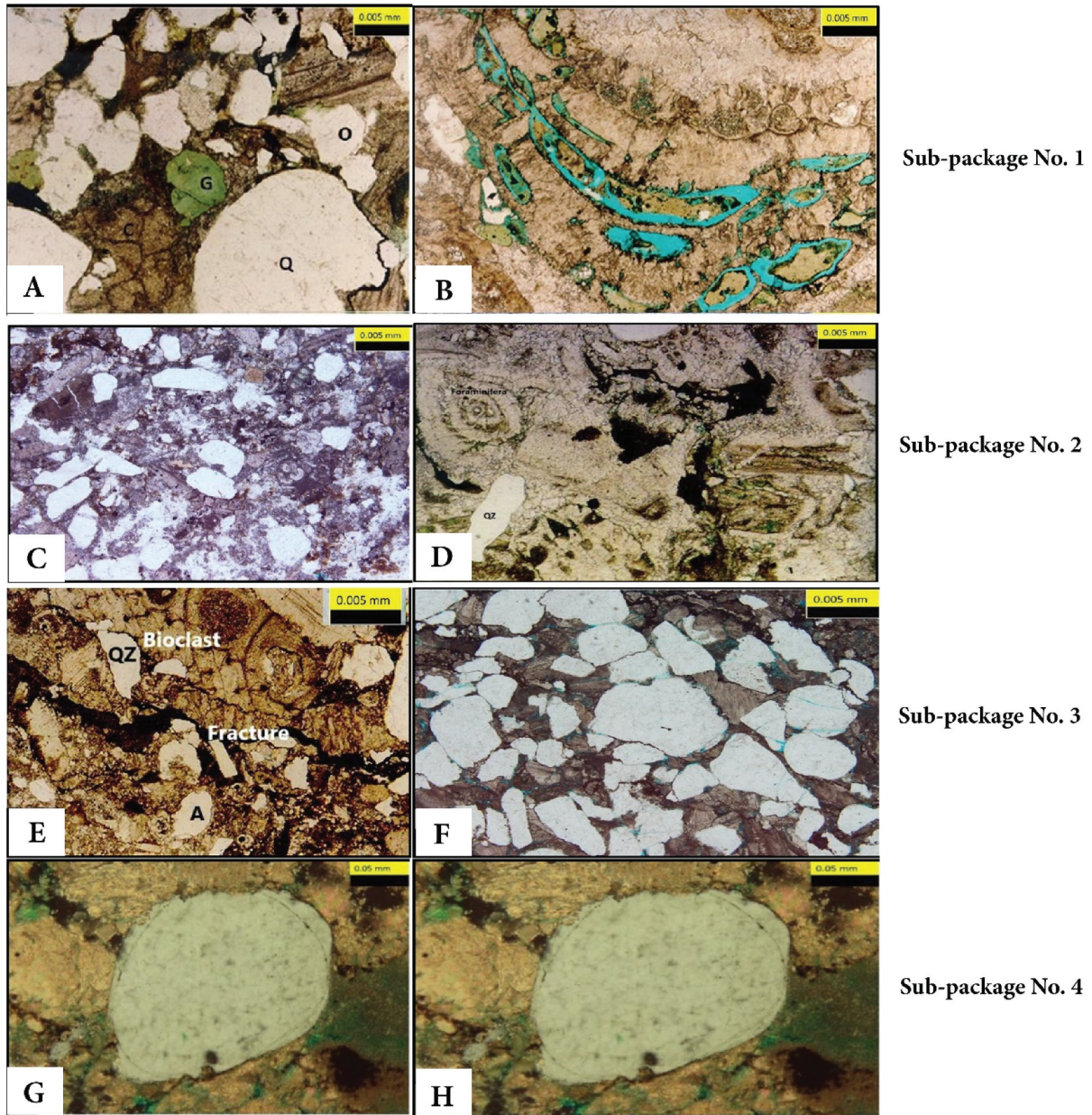
Figure 9. Core chips thin sections photomicrographs in GS184-4A well (a) Sample at depth 11,419.5 ft. shows Q. the corrosive action of calcite cement for QZ grains, C. spary calcite cement, O. siliceous overgrowth cement and G. glauconite. (b) A thin section at a depth of 11,423 ft., shows QZ grains, glauconite, micritic calcite cement, moldic porosity and bryozoa bioclast. (c) A thin section at 11,390 ft. shows QZ grains embedded in micritic cement in polarized light. (d) A thin section at a depth of 11,405 ft. shows foraminifera, traces QZ, glauconite, micritic calcite cement, and polarized light. (e) Sample at depth 11,353 ft. shows fracture-filled by pyrite, A. siliceous overgrowth cement, polarized light. (f) Photomicrograph at a depth of 11,372 ft. shows quartz grains with calcite cement, polarized and crossed polarized light. (g) Photomicrograph at a depth of 11,335 ft. shows siliceous overgrowth cement crossed polarized. (h) A thin section at a depth of 11,341 ft. shows well-sorted sandstone with intergranular porosity, crossed polarized: magnification 40X.

$$\Phi_{Ncorr} = \Phi_N - (V_{sh} * \Phi_{Nsh}) \qquad (3)$$

Where $_{Ncorr}$ is the corrected porosity for clean rock from shale and Φ_{Nsh} is the neutron porosity value for shale

$$\Phi_D = \frac{(\rho_{ma} - \rho_b)}{(\rho_{ma} - \rho_f)} \qquad (4)$$

Then, the effective porosity (Φ_e) was calculated by the equation (3)equation (5) of Schlumberger (1998) from the average total porosity.

$$\Phi_e = \Phi_t * (1 - V_{sh}) \qquad (5)$$

Where ρ_{ma} is the density of the matrix, ρ_b is the bulk density measured from the log, ρ_f is the fluid density, Φ_t is the total porosity which is the average value
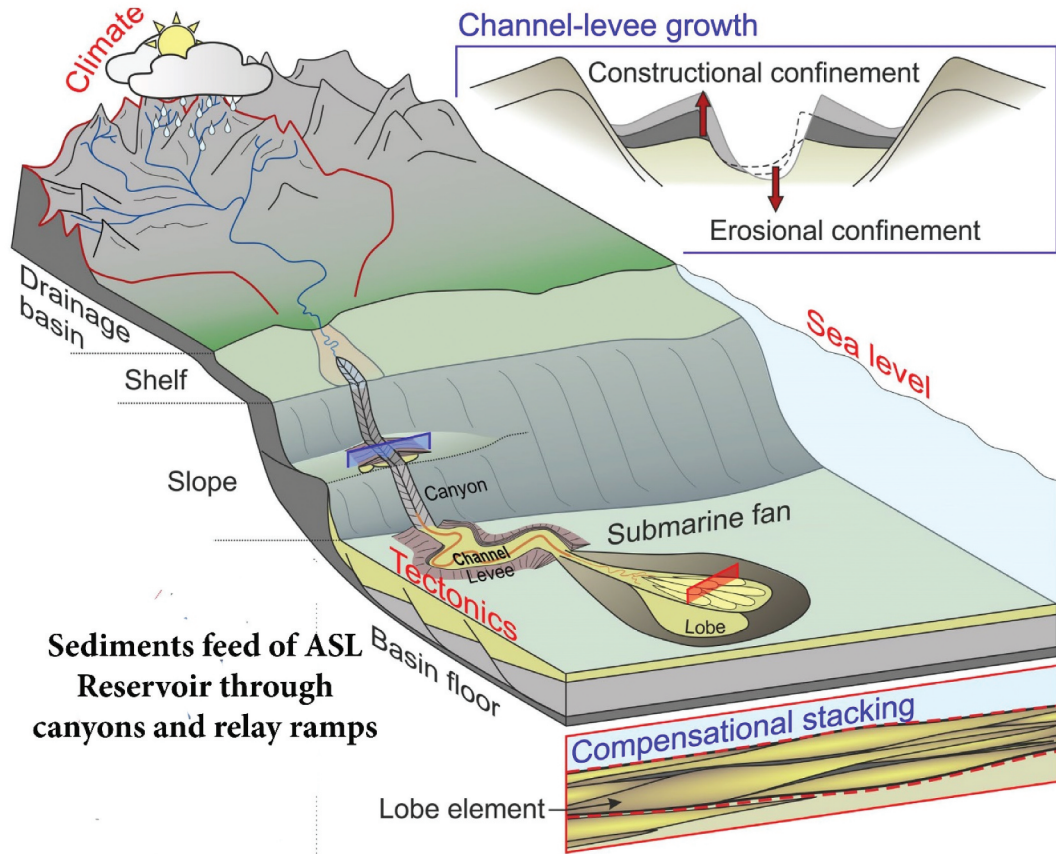
Figure 10. Schematic image of ASL reservoir built on typical submarine fans (after Prélat et al. (2009), Sømme et al. (2009), Ferguson et al. (2020)).

of Φ_{Ncorr} and Φ_D, and Φ_e is effective porosity.

The determination of Water Saturation employed Archie's equation (eq. 6), proving its applicability even in reservoirs with varying shale content. However, the calculation of water saturation was disregarded within the bad-hole intervals, marked by the bad-hole flag. This omission was due to the adverse impact of the hole on micro-resistivity measurements and the density tool.

$$S_w = \left[\left(\frac{a}{Fm} \right) * \left(\frac{R_w}{R_t} \right) \right]^{\left(\frac{1}{n} \right)} \qquad (6)$$

S_w refers to water saturation, Fm for the formation factor ($Fm = 1/m$), R_w for the ohmmeter, R_t for the observed deep resistivity, and (a, b, and c) for Archie's coefficients, which are obtained from the Pickett plot.

We used the empirical equation (7) provided by Wyllie and Rose (1950) to calculate the permeability of the reservoirs.

$$K = \left(250 * \left(\frac{\Phi^3}{S_{wir}} \right) \right)^2 \qquad (8)$$

Where S_{wir} denotes irreducible water saturation, porosity, and permeability in millidarcy (mD). The amount of water in the oil zone determined by equation (8) is the irreducible water saturation.

$$S_{wir} = [C/(\Phi/(1 - V_{sh}))] \qquad (8)$$

Where C is Buckles's constant.

3.3. Petrographic description of thin sections

Petrography is a branch of petrology that focuses on detailed descriptions of rocks, such as mineral content and textural relationships. ASL reservoir in the study area is fully described in thin sections from cored intervals in GS184-4A well and ditch cuttings in OCT-J7B, GS173–2 and GS195–5 wells. This description resulted in having two distinctive facies, which are carbonates, and siliciclastics, siliciclastics are mainly sandstones and are not classified in our study. Still, we used the Wentworth (Williams et al. 2006) scale to find the appropriate grain size name, while carbonates are classified according to Dunham's classification Dunham (1962) and its modification by Embry and Klovan (1971).

3.4. Core analysis

The core analysis involves cleaning, slabbing, and measuring porosity, horizontal permeability, and grain density. After taking cores out of fibreglass tubes, they are marked with longitudinal red and
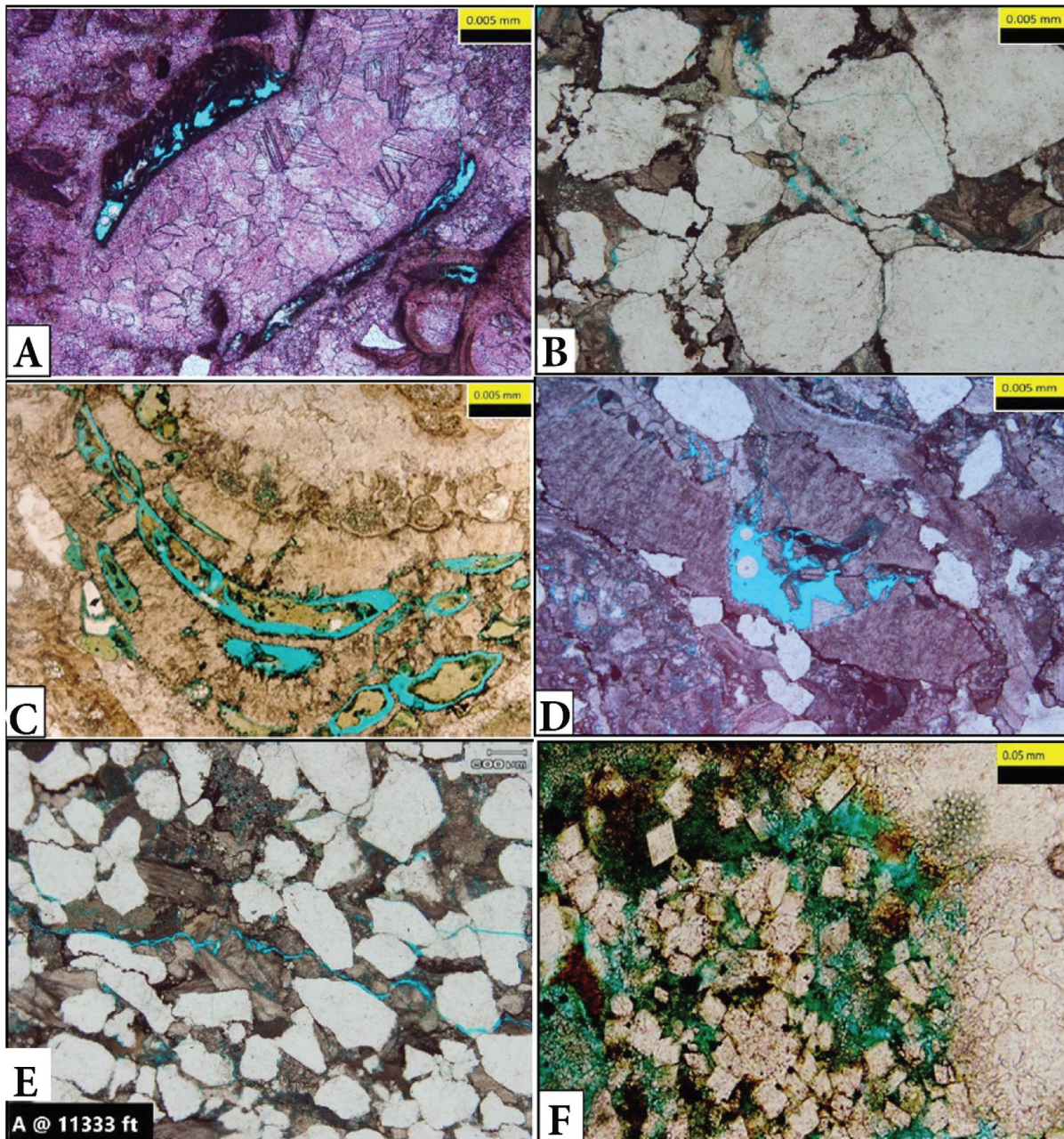
Figure 11. Core chips thin sections photomicrographs in GS184-4A well, (A) Highlight moldic spary calcite cementation at depth 11,330 ft., polarized. (B) Photomicrograph highlights compaction at a depth of 11,333 ft., polarized light. (C) Thin section highlights moldic porosity due to the leaching of skeletal grains at a depth of 11,423 ft., polarized light. (D) Thin section shows the dissolution of skeletal grain and polarized light. (E) Section highlights fractures at a depth of 11,333 ft., polarized light, and (F) Thin sections photomicrograph at a depth of 11,363 ft., highlight selective dolomitization which enhanced porosity, polarized light: magnification 200X.

blue lines for orientation control and marked transversally with yellow lines for each foot depth interval. Depth intervals and recovered cores are re-checked and compared with field data, and core gamma is re-measured for quality control. The core of the GS184-4A well was visually examined, and descriptions were recorded at a 1:50 ft. scale. The depth shift was determined and modified according to a comparison of the well logs' depth and the core depth. The chemical rock composition of the main constituents was discriminated from the bottom towards the top depth. The complete physical composition of every individual rock unit

was determined with considerateness of accurate grain size, roundness, grain sorting, grain fabric, grain orientation, grain imbrication and visible accessory minerals. The grading patterns of every sedimentary cycle were determined and described.

4. Results and discussion

4.1. Structure regime of the area

GS184-4A is well tying actual formation tops with interpreted seismic reflectors. The most common manual picking technique is interpreting horizons

on lines, cross-lines, time slices, and traverses by hand, but it is the least efficient in terms of interpreter time and effort. The main October growth fault without interpretation (Figure 4a) and the seismic attribute were essential in defining the structure. All types of attributes are tested for the seismic volume. It found that RMS amplitude, structure smoothing, and variance as structure attributes, coherence as a horizon attribute, and sweetness as a stratigraphic attribute are the best to apply for this seismic volume. Fault interpretation is one of the essential steps in seismic interpretation and is based on discontinuities in the reflection, disclosures in tying reflections around loops, divergence in dip unrelated to stratigraphy and diffraction patterns, and distortion or disappearance of reflections below suspected fault lines (Figure 4b). Seismic edge-detection methods are used to conduct stratigraphic and structural interpretations of desired geologic features in seismic data.

The Electric log correlation was carried out for the entire stratigraphic section drilled in the four wells from the surface to total depth (Figure 5). The correlation shows that the first two northern wells penetrated the Pre-Miocene section with potential fault contact between the Miocene and the Pre-Miocene sections. On the other hand, the other two wells were drilled only to a total depth within the Rudeis section without encountering the Pre-Miocene section. A more focused and detailed correlation with particular emphasis on the ASL reservoir section within the Upper Rudeis Formation was carried out across a northwest-southeast section for the four wells used in the study area (Figure 6). The correlation shows thickness variation occurring within the ASL reservoir section and also a potential high reservoir quality turning into more calcareous sandstone with low reservoir quality from northwestern wells to southeastern ones.

Structural cross-sections and maps were used to build a complete structural geologic model accurately, which was translated into mapping at three levels. The structural mapping at the South Gharib level, derived from seismic data and incorporating all picks from well controls, indicated that all wells in the study area were drilled on the downthrown side of the major Clysmic trending fault "A" with 600–800 feet of the throw. In contrast, the mapping at the Feiran level indicates that all wells in the study area were drilled on the downthrown side of the major Clysmic trending faults "A" and "B" with throw ranges from 1200 to 1400 feet, respectively (Figure 7). Also, the structural mapping at ASL Member shows that the wells in the study area were drilled on the downthrown side of the

Clysmic trending faults, OCT-J7B well down to fault "B", GS184-4A down to fault "A" and GS195–3 well down to fault "D". On the other hand, GS173–2 well was drilled on the footwall of fault "A" this is the reason for lack of sand in this well (Figure 7).

The dip structural section across the northern well OCT-J7B shows that the well was drilled entirely on the downthrown side of the Clysmic trending faults "A" and "B" at South Gharib Formation, Belayim Formation and ASL Member (Figure 8, A-A'). The northern well GS173–2 shows that thick sand (168 ft.) was found in the well, and the lateral seal of the reservoir is the Hawara shale and older shales of the Rudeis section (Figure 8, B-B'). The dip structural section across the southern well GS184-4A shows that the well was drilled on the downthrown side of the Clysmic trending faults "A" and "D" at South Gharib Formation, Belayim Formation and ASL Member (Figure 8, C-C'). The dip structural section across the southern well GS195–3 shows that the well was drilled on the downthrown side of the Clysmic trending fault "D" at South Gharib Formation, Belayim Formation and ASL Member (Figure 8, D-D').

4.2. Facies analysis of ASL member

The lithology identification and facies analysis of ASL Member in GS184-4A well is based on petrographic examination of core chips thin sections and ditch cutting description of the interval that was not cored. The non-cored interval from 10,998 to 11,330 ft. consists mainly of limestone interbedded with shale and sandstone streaks. ASL Member is a thick 95 ft. package with three entirely and one partially cored dirtying fining upwards sub-packages arranged from bottom to top. Each sub-package is subdivided into two discrete elements, Type-A and Type-B lithofacies. Type-A consists of sandy grainstone and packstone interbedded with poorly sorted, medium to coarse-grained sandstones and calcareous sandstones. Bed contacts are typically planner or rarely erosive and loaded and often have mud clasts, skeletal fragments, or quartz granules concentrated towards their bases. Skeletal allochems are abundant throughout this element and comprise bivalve, bryozoan, gastropod, red algal, and echinoid fragments. Type-B elements occur at the top of each sub-packages and are comprised of clay-rich sandy skeletal packstones that have a gradational contact with the underlying Type-A elements. Quartz granules and skeletal debris are concentrated in coarser, cleaner laminations, and microfacies analysis reveals that planktonic foraminifera is particularly abundant. Thin sections
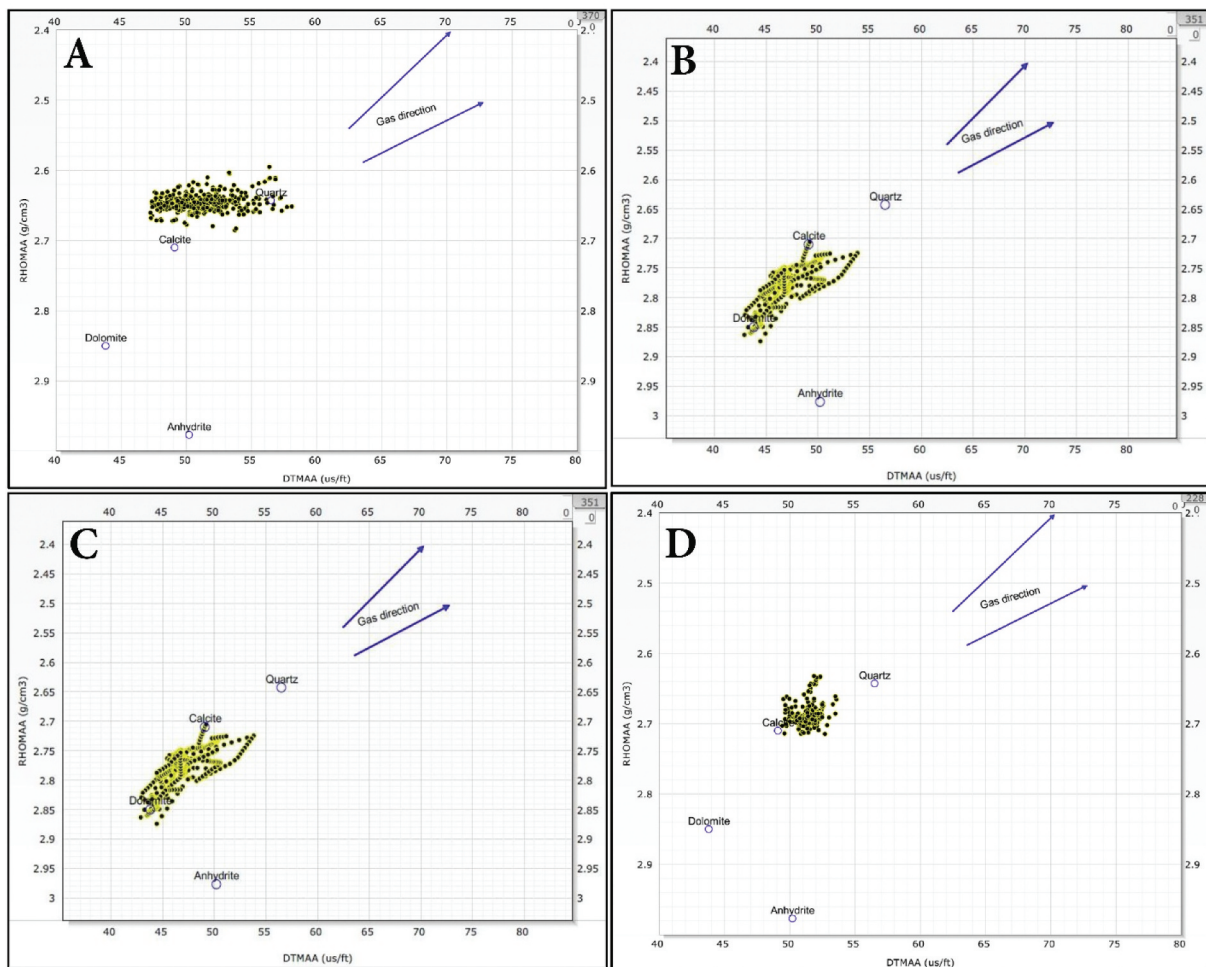
Figure 12. MID lithology crossplot for ASL member in (A) OCT-J7B well, (B) GS173–2 well, (C) GS184-4A well, and (D) GS195–3 well.

Table 1. ASL reservoir summary for the study area.

Wells	Formation	Flag Name	Top ft	Bottom ft	Gross ft	Net ft	Net to Gross %
OCT-J7B	ASL_SAND	Reservoir	9683	9849	166	150	90
		Pay				90	54
GS173–2		Reservoir	8200	8268	68	26	39
		Pay				0	0
GS184-4A		Reservoir	10929	11124	195	163	84
		Pay				62	32
GS195–3		Reservoir	10439	10621	181	166	92
		Pay				22	12

from the cored interval are stressed mainly on Type-A as it comprises high reservoir quality.

This sub-package (11,425–11,410) consists of 15 ft. of sandy skeletal grainstone with some streaks of calcareous sandstone overlaid by sandy skeletal packstone. The core chip's thin sections are composed of various sizes of skeletal grains of planktonic foraminifera, bivalves, bryozoa and algae with micritic and aspartic calcite cement, with traces of glauconite grains, with vuggy and moldic porosity (Figure 9a,b). Sub-packing No.2 (11,410–11,385) represents 25 ft. and consists mainly of sandy skeletal packstone underlain by intercalations of sandy skeletal grainstone and calcareous sandstone. The thin sections are composed of various sizes of skeletal grains, with fine-grained QZ grains, micritic cement, and traces of glauconite grains, with vuggy and moldic porosity (Figure 9c,d). Sub-package No.3 (11,385 to 11,343 ft.) is the thickest of 142 ft. and consists mainly of sandy skeletal grainstone with some intercalations of calcareous sandstone and overlaid by highly fractured, stylolitic, and bioturbated sandy skeletal wackestone (Figure 9e,f). Sub-package No.4 (11,343–11,330) represents facies of Type-A only, which is about 13 ft. It consists of skeletal grainstone intercalated with calcareous sandstone, sandy skeletal grainstone, and packstone. The
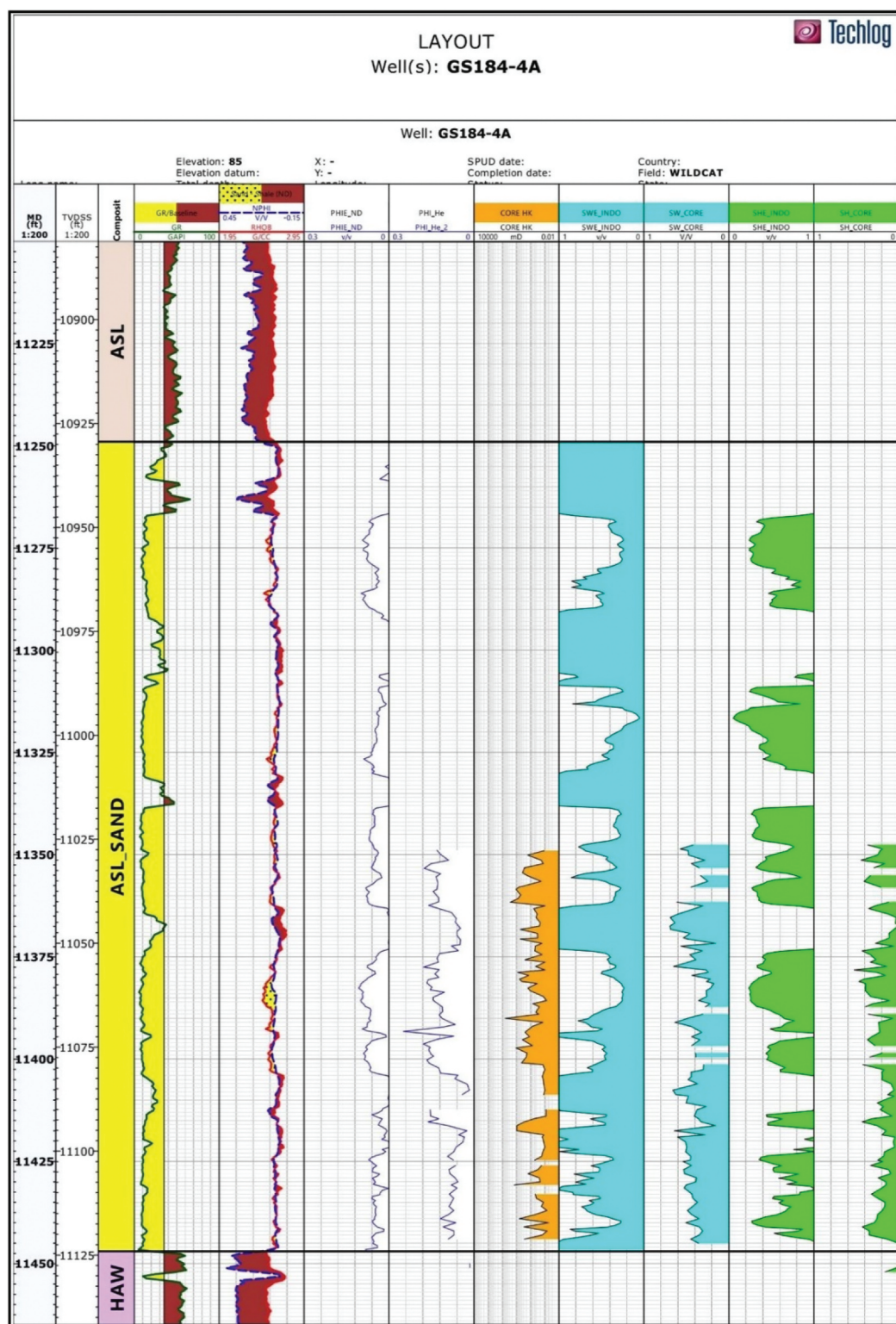
Figure 13. The qualitative relationship between core-measured parameters (helium porosity, horizontal permeability, water, and hydrocarbon saturations) and the corresponding log-derived parameters.

calcareous Sandstone is sub-mature, glauconitic, and pyritic, with shell fragments, spary calcite and micrite cement, and intergranular and intra-granular porosity (Figure 9g,h).

The normally graded, fining upward nature of the beds and the presence of mud clasts in the lithology of Type-A elements suggest rapid deposition from high-density turbidity currents. In contrast, Type-B elements' bioturbated, mud-prone nature indicates lower energies and less erosive turbidity currents. The alternation of clastic and carbonate material within the package reflects a dual sediment source. Each sub-package is interpreted in this context to represent an abrupt influx of high-energy turbidities on a submarine fan, where fault reactivation is likely to have precipitated lobe rejuvenation (Type-A
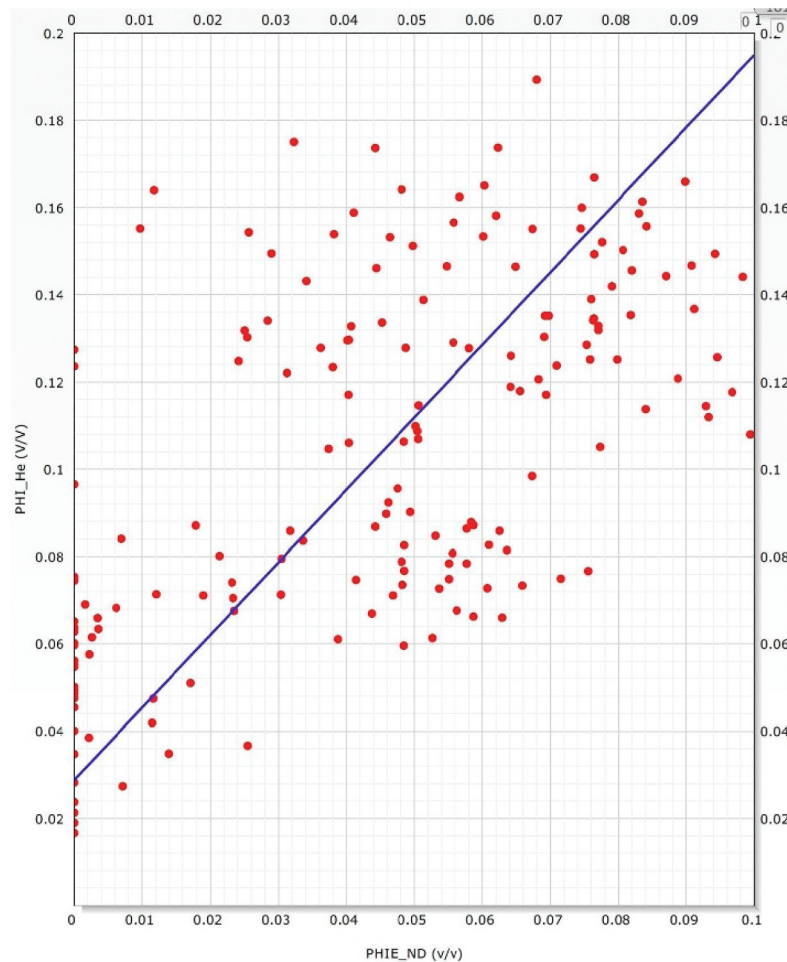
Figure 14. Core helium porosity and log-derived effective porosity relationship.

elements). Most turbidity currents eventually bypass the lobe due to the infill of the available accommodation space, resulting in lower energy marginal and/or distal deposition (Type-B elements) (Figure 10).

The thickness of the ASL Member in the OCT-J7B well is 235 ft. which consists mainly of sandstone with limestone and shale streaks. The thickness of ASL Member in GS173–2 well is 220 ft. and 70 ft. net sandstone thickness, consisting mainly of limestone with intercalations of sandstones and shale. The limestone's lithology is described as off-white, cryptocrystalline to very fine crystalline, hard to moderately hard, argillaceous to extremely argillaceous, infrequently sandy, with no discernible porosity, and typically with little chance of hydrocarbon evaluation.

4.3. Diagenesis and reservoir quality of ASL member

Diagenesis is a broad spectrum of physical, geochemical and biological post-depositional processes by which original sedimentary mineral assemblages and their interstitial pore waters interact in an attempt to reach textural and thermodynamic equilibrium with their environment (Burley and WORDEN 2003).

Reservoir quality is one of the critical controls on prospectivity during petroleum exploration. Therefore, it is crucial to have a detailed understanding of what controls reservoir quality to assist with appraising the economic viability of petroleum discoveries (Selley 1997). Cementation is the main reservoir quality-reducing factor that causes loss of pore volume with progressive cementation and pore filling (Figure 11a). Compaction is an essential process leading to forming a consolidated rock, with calcite being the sandstone's most common cement (Figure 11b). Overburden pressure leads to bed thinning in sedimentary rocks, expelling intergranular fluids, closer packing of grains, and porosity reduction. Diagenetic processes such as dissolution, fracturing, and selective dolomitisation of calcite cement enhance the porosity and permeability of ASL Member sandstones in the GS184-4A well (Figure 11c).

4.4. Petrophysical evaluation of ASL member

The optimal cut-offs for net pay estimation for ASL Members have been identified and applied to the petrophysical evaluation using actual production data from the research region. Shale
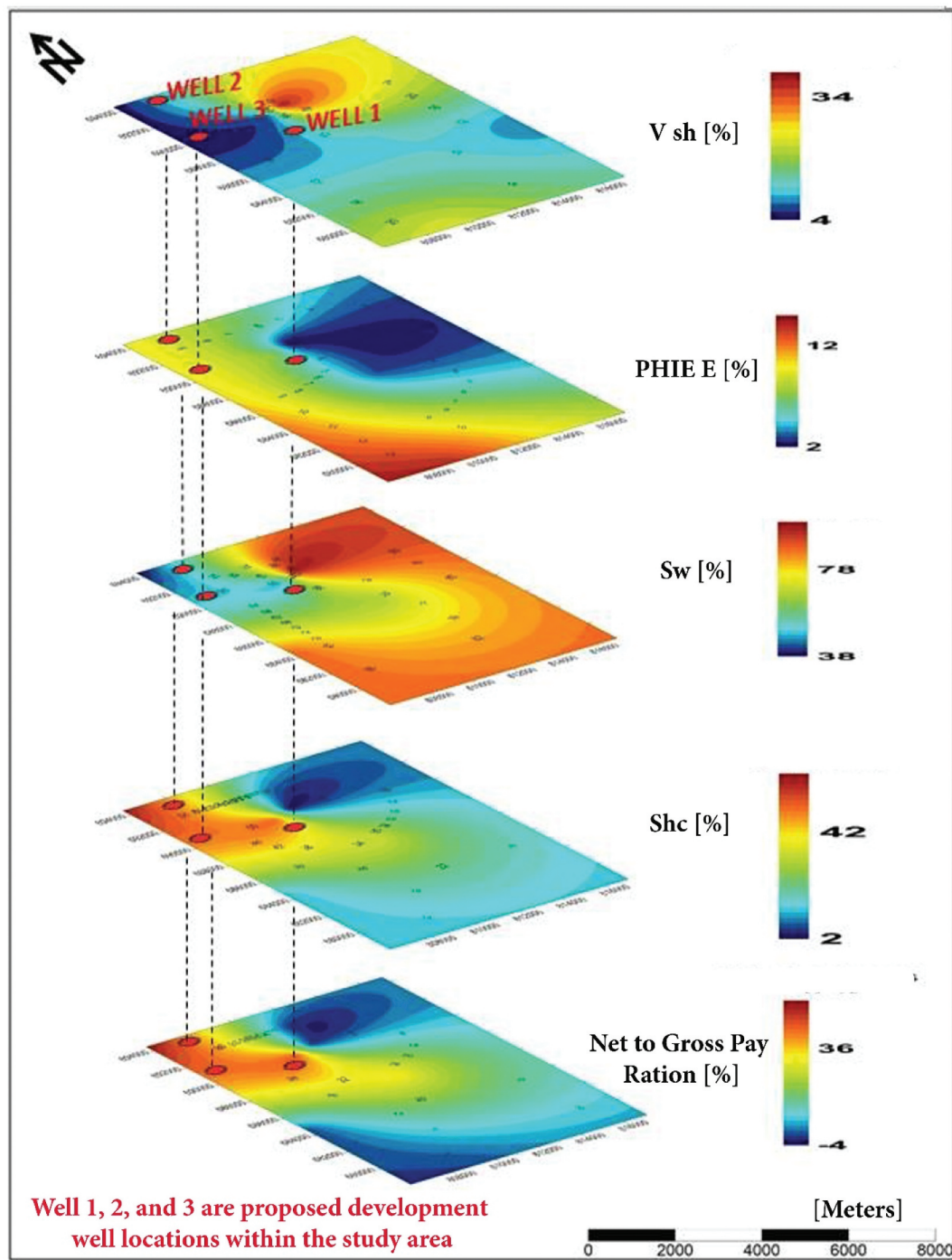
Figure 15. Composite petrophysical parameters maps of ASL Reservoir.

volume "35%" and effective porosity "10%" for estimating gross reservoirs and water saturation cut-off "50%" for estimating net pay relative to gross reservoirs are these cut-offs. Figure 12 shows the results of the net reservoir and net pay for each well individually, while Table 1 summarises the ASL reservoir in the research region.

The depth between the two was compared using the wireline gamma ray log in the GS184-4A well and the core gamma ray log that was recorded after the coring procedure. This depth-matching technique is required to link measurements from cores and logs. Figure 13 depicts a qualitative relationship between core-measured parameters (helium porosity, horizontal permeability, water, and hydrocarbon saturations) and the corresponding log-derived parameters, except for permeability, which is highly predictable in non-cored wells when using reservoir rock typing (Amaefule et al. 1993). Nevertheless, statistical comparison between core and log data is as trustworthy as qualitative. The log-derived effective porosity is typically lower than the core helium porosity (neutron density method). Core plug measurements of water and hydrocarbon saturations are lower than those

Table 2. Proposed new development wells in the area of study.

Target Coordinates	Well 1	Well 2	Well 3
X	810312	807124	806506
Y	689845	693545	691872
Predicted Reservoir Parameters			
Shale Volume %	10–14	4–6	4–8
Effective Porosity %	10–12	8–10	6–7
Hydrocarbon Saturation %	50–54	54–58	42–46
Net to Gross Pay %	40–44	48–52	46–52

calculated from logs. This might be explained by some gases caught in the pores during the escaping laboratory measurements.

The discovered associations could be utilised to compare the reservoir parameters derived from logs to those measured in core plugs (Figure 13). Therefore, the best-fit line equation was selected to delineate the core parameters within the non-cored intervals of the ASL Member reservoir in the study wells, such as (Figures 13 and 14), which shows calculated effective porosity by neutron density method plotted versus core helium porosity. It's obtained that the helium porosity increases to a degree that can be considered a fixed percentage or a fixed factor over its counterpart calculated from neutron well log. As a result, the best-fit relationship between these two variables can be expressed by the following:

$$\emptyset_H = 1.662 * \emptyset_{Eff.} + 0.037$$

Where:
$\emptyset_H$: Core helium porosity
$\emptyset_{Eff.}$: Log calculated effective porosity.
R: Correlation coefficient ($R = 0.617$)

The mapped values of shale volume, effective porosity, water saturation, hydrocarbon saturation, and net-to-gross pay ratio can be combined to highlight the horizontal variation of these parameters (Figure 15), leading to directions of the best reservoir quality. Shale volume is the most critical factor affecting the reservoir quality and has a destructive effect on porosity. We can notice that shale volume decreases towards the northwestern direction at OCT-J7B well and increases to reach its maximum value at GS173–2 well in the northeastern direction. Effective porosity increases in the southwest direction, which records about 14% and decreases to 2% at GS173–2 well. The Water saturation reflects the amount of water entrapped in the reservoir pores. The effective water saturation was mapped for the ASL Member in the study area and revealed that the maximum water saturation has two directions, the northeastern direction at the GS173–2 well and the southwestern direction, while the minimum

water saturation was recorded at OCT-J7B well. In contrast, the maximum hydrocarbon saturation, which reaches about 60%, appears in the northwestern direction at the OCT-J7B well. Finally, the net-to-gross ratio was also mapped and showed that the maximum pay appears to have the northwestern direction. Finally, following up on some potential well locations is recommended as they might bear oil potential from the interpretation carried out in this study (Figure 15). Well locations and predicted reservoir parameters are summarised in Table 2.

5. Conclusions

This study addressed an integration between sedimentological and petrophysical techniques applied to ASL Member as one of the main producing rock units in the Early-Middle Miocene age in October Field. The Electric log correlation showed that the first two northern wells (OCT-J7B and GS173–2) penetrated the Pre-Miocene section, while the other two wells (GS184-4A and GS195–3) were drilled only to a total depth within the Rudeis section. The dip structural sections across the four wells indicated that all wells were drilled on the downthrown side of the main Clysmic trending fault. The lateral seal of the reservoir is the Hawara shale, while the vertical seal is the Lagia shale. ASL Member consists mainly of limestone intercalated with shale and sandstone streaks and can be subdivided into three completely and one partially cored dirtying fining upwards sub-packages. Type-A and Type-B lithofacies occur at the base of each sub-package. Type-A consists of sandy grainstone and packstone interbedded with poorly sorted, medium to coarse-grained sandstones and calcareous sandstones. Sub-packages 3 and 4 are of good reservoir quality due to diagenetic processes such as fractures and dolomitisation. The routine core analysis data of ASL Member in GS184-4A well was used to study the relationships between the reservoir parameters (i.e. vertical and horizontal permeability, helium porosity and grain density). The grain density values vary from 2.65 gm/cm3 to 2.81 g/cm3, and the helium porosity values vary from 1.65% to 25%, with an average of 10.8%. The nitrogen permeability values in the horizontal direction vary from 0.06 mD to 60.41

mD, while the vertical permeability values range from 0.003 mD to 4.13 mD. The average calculated shale volume from the density-neutron method was between 6% and 38%, while the average calculated effective porosity from the same method was between 2% and 10%. The final average volume of shale ranged from 4% to 38%, with a decreasing trend in the northwestern direction towards OCT-J7B well and an increase in the southwestern direction. Recommendations include avoiding uplifted fault blocks, performing reservoir rock typing for the ASL Member, and following up on potential well locations for oil potential.

Acknowledgments

Disclosure statement

ORCID

Ahmed Diab 🆔 http://orcid.org/0000-0002-8327-7333
Hossam M. El-Sayed 🆔 http://orcid.org/0000-0003-0808-7350

References

Abdel Fattah TH, Diab A, Younes M, Ewida H. 2020. Improvement of Gulf of Suez subsurface image under the salt layers through re-processing of seismic data-a case study. NRIAG J Astron Geophys. 9(1):38–51. doi: 10.1080/20909977.2020.1711575.

Abdel-Fattah TA, Rashed MA, Diab AI. 2019. Reservoir compartmentalization phenomenon for lower safa reservoir, obaiyed gas field, north western desert, Egypt. Arabian J Geosci. 12(22):1–13. doi: 10.1007/s12517-019-4853-7.

Abdine S, Homossani A, Lelek J, 1992. October field the latest giant under development in the Gulf of Suez, Egypt, in Sadek A, editor, Geology of the Arab World: Proceedings 1st International Conference on Geology of the Arab World, Cairo, v. 1, p. 61–85.

Aly SA, Ewida HF, Shebl A, Nasr IA. 2015. Well log analysis and oil potentialities of the lower cretaceous nubia sandstones, west Esh El mallaha oilfield, southern Gulf of Suez, Egypt. Egyptian J Pure Applied Sci. 1–11.

Amaefule JO, Altunbay M, Kersey DG, Keelan DK. 1993. Enhanced reservoir description: using core and log data to identify hydraulic (flow) units and predict permeability in uncored Intervals/Wells. SPE 26436.

Bevan TG, Moustafa AR. 2012. Inverted rift basins of northern Egypt. In: Roberts DG, Bally BW, editors. Regional Geology and Tectonics: Phanerozoic Rift Systems and Sedimentary Basins. Vol. 1. Amsterdam, The Netherlands: Elsevier; p. 482–507. doi: 10.1016/B978-0-444-56356-9.00018-3.

Bosworth W. 1994. A model for the three-dimensional evolution of continental rift basins, north-east Africa. In: Schandelmeier H, Stern RJ, editors. Geology of Northeast Africa (part 2), Geol. Rundsch. Vol. 83. Verlag: Springer; p. 671–688.

Bosworth W, Crevello P, Winn RD, Steinmetz J. 1998. Structure, sedimentation, and basin dynamics during rifting of the Gulf of Suez and north-western Red Sea. In: Purser B, Bosence D, editors. Sedimentation and Tectonics in Rift Basins Red Sea:- Gulf of Aden. Dordrecht: Springer. doi: 10.1007/978-94-011-4930-3_6.

Bosworth W, McClay K. 2001. In: Ziegler PA, Cavazza W, Robertson AHF, Crasquin-Soleau S, editors. Structural and stratigraphic evolution of the Gulf of Suez rift, Egypt: A synthesis. Vol. 186. Paris: Mémoires du Muséum national d'Histoire naturelle; p. 567–606.

Burley SD, WORDEN RH. 2003. In: Burley, SD, Worden, R.H., Eds. Sandstone. In Sandstone Diagenesis; recent and, ancient. Vol. 4. Malden, MA, USA: Blackwell Publishing; p. 3–44.

Davies Q, Bliefnick D, 2001. Sedimentology and depositional setting of the Asl and hawara members, October Field, Egypt, Badley Ashton reservoir geoscience.

Diab AI, Khalil HM. 2021. Quantitative assessment of the tight gas reservoirs in the Obaiyed field, Shushan Basin, NW Egypt. NRIAG J Astron Geophys. 10(1):320–332. doi: 10.1080/20909977.2021.1929745.

Dunham RJ. 1962. Classification of carbonate rocks according to depositional texture. In: classification of carbonate rocks (ed. W.E. Ham). Am Assoc Pet Geol Mem. 1:108–121.

El-Dakak MA, Abdelfattah TA, Diab AI, Kassem MA, Knapp CC. 2021. Integration of borehole depth imaging and seismic reflection results in reservoir delineation: an example from the alam El bueib 3C field, northern western desert, Egypt. J Afr Earth Sci. 184:104322. doi: 10.1016/j.jafrearsci.2021.104322.

El Ghamri MA, Warburton IC, Burley SD. 2002. Hydrocarbon generation and charging in the October field, gulf of Suez, Egypt. J Pet Geol. 25(4):433–464. doi: 10.1111/j.1747-5457.2002.tb00094.x.

El-Shahat W, Villinski JC, El-Bakry G. 2009. Hydrocarbon potentiality, burial history and thermal evolution for some source rocks in October oil field, northern Gulf of Suez, Egypt. J Pet Sci Eng. 68(3–4):245–267. doi: 10.1016/j.petrol.2009.06.018.

Embry AF, Klovan JE. 1971. A Late devonian reef tract on northeastern banks Island, N.W.T. Bull Can Petrol Geol. 19(4): 730–781. ISSN 0007-4802.

Ferguson RA, Kane IA, Eggenhuisen JT, Pohl F, Tilston M, Spychala YT, Brunt RL. 2020. Entangled external and internal controls on submarine fan evolution: an experimental perspective. The Depositional Record. 6(3):605–624. doi: 10.1002/dep2.109.

Garfunkel RL, Bartov Y. 1977. The tectonic of the Suez rift. – geological survey of Israel. Bulletin. 71:1–44.

Jarrige J-J, Ott D'estevou P, Burollet PF, Montenat C, Prat P, Richert J-P, Thiriet J-P. 1990. The multistage tectonic evolution of the Gulf of Suez and northern red sea continental rift from field observations. Tectonics. 9(3):441–465. doi: 10.1029/TC009i003p00441.

Kröner A. 1984. Late Precambrian plate tectonics and orogeny: a need to redefine the term pan-african. In: Klerkx J, and Michot J, editors African geology. Tervuren: Musée. R. l'Afrique Centrale; p. 23–28.

Kröner A. 1993. The Pan African belt of northeastern and Eastern Africa, Madagascar, southern India, Sri Lanka and East Antarctica: terrane amalgamation during the formation of the Gondwana supercontinent. In: Thorweihe U, and Schandelmeier H, editors. Geoscientific research in Northeast Africa. Balkema, Rotterdam: CRC Press; p. 3–9.

Lashin A, Al-Arifi N, Abu Ashour N. 2011. تقييم تكويني "عسل" و "هواره" باستخدام خواص مشتقه من البيانات السيزمية و تسجيلات الآبار ، حقل أكتوبر للزيت، خليج السويس-مصر. Arabian J Geosci. 4(3–4):365–383. doi: 10.1007/s12517-009-0065-x.

Lelek JJ, Shepherd DB, Stone DM, Abdine AS. 1992. October field - the latest giant under development in Egypt's gulf of suez. In: Halbouty MT, editor. Giant Oil and gas fields of the Decade 1978-1988. Tulsa, Oklahoma, USA: American Association of Petroleum Geologists; p. 231–249.

Liner C. 2004. Elements of 3D seismology. 3rd ed. Tulsa, Oklahoma: PennWell; p. 608.

Lyberis N. 1988. Tectonic evolution of the Gulf of Suez and the Gulf of Aqaba. Tectonophysics. 153(1–4):209–220. doi: 10.1016/0040-1951(88)90016-9.

Mercaroni D2014. The effect of Vshale 3D distribution on the secondary migration of hydrocarbons. PHD Thesis, University of Padua; p. 158.

Montenat C, D'estevou O, Jarrige JJ, Richert JP. 1998. Rift development in the Gulf of Suez and the north-western 180 hydrocarbon potential in the Gulf of Suez rift Basin (Egypt) Red Sea: structural aspects and related sedimentary processes. In: Purser BH, and Bosence DWJ, editors Sedimentation and tectonics of rift basins: red sea–Gulf of Aden. London: Chapman and Hall; p. 97–116.

Moustafa AR, Khalil MH. 1995. Superposed deformation in the northern Suez rift, Egypt: relevance to hydrocarbon exploration. J Pet Geol. 18(3):245–266. doi: 10.1111/j.1747-5457.1995.tb00905.x.

Patton TL, Moustafa AR, Nelson RA, Abdine SA. 1994. Tectonic evolution and structural setting of the suez rift. In: London SM, editor. Interior rift basins. Vol. 59. Tulsa, Oklahoma, USA: American Association of Petroleum Geologists; p. 7–55.

Peijs JAMM, Bevan TG, Piombino JT. 2012. Regional geology and tectonics: phanerozoic rift systems and sedimentary basins: the gulf of Suez rift basin. Elsevier. 1B:166–188.

Prélat A, Hodgson DM, Flint SS. 2009. Evolution, architecture and hierarchy of distributary deep☐water deposits: a high☐resolution outcrop investigation from the Permian Karoo Basin, South Africa. Sedimentology. 56(7):2132–2154. doi: 10.1111/j.1365-3091.2009.01073.x.

Robson DA. 1971. The structure of the Gulf of Suez (clysmic) rift, with special reference to the eastern side. JGS. 127(3):247–271. doi: 10.1144/gsjgs.127.3.0247.

Said R. 1990a. Cenozoic. In: Said R, editor The geology of Egypt. Netherlands: Balkema, Rotterdam; p. 451–486.

Said R. 1990b. Cretaceous paleogeographic maps. In: Said R, editor The geology of Egypt. Balkema, Rotterdam; p. 439–449.

Schlumberger. 1998. Cased hole log interpretation Principles/Applications. Houston: Schlumberger Wireline and Testing; p. 198.

Selley RC. 1997. Elements of petroleum geology. 2nd revised ed. Amsterdam, The Netherlands: Elsevier Science Publishing Co Inc.; p. 470.

Sømme TO, Helland☐Hansen W, Martinsen OJ, Thurmond JB. 2009. Relationships between morphological and sedimentological parameters in source☐to☐sink systems: a basis for predicting semi☐quantitative characteristics in subsurface systems. Basin Res. 21(4):361–387. doi: 10.1111/j.1365-2117.2009.00397.x.

Stern RJ. 1981. Petrogenesis and tectonic setting of late precambrian ensimatic volcanic rocks, central eastern desert of Egypt. Precambrian Res. 16(3):195–230. doi: 10.1016/0301-9268(81)90013-9.

Stern RJ. 1994. Arc assembly and continental collision in the Neoproterozoic East African orogen: implications for the consolidation of Gondwanaland. Annu Rev Earth Planet Sci. 22(1):319–351. doi: 10.1146/annurev.ea.22.050194.001535.

Stoeser DB, Camp VE. 1985. Pan African microplate accretion of the Arabian shield. Geol Soc Am Bull. 96(7):817–826. doi: 10.1130/0016-7606(1985)96<817:PMAOTA>2.0.CO;2.

Stone DM. 1992. Reservoir potential of the asl formation (miocene) north October field, Gulf of Suez, Egypt, internal petrophysics project report. Amoco Production Company. 1:194–228.

Temraz M, Dypvik H. 2017. The lower miocene nukhul formation, Gulf of Suez, Egypt: microfacies and reservoir characteristics, springer. J Petrol Explor Prod Technol. 8(1):1–13. doi: 10.1007/s13202-017-0386-3.

Tiab D, Donaldson EC. 2015. Petrophysics: theory and practice of measuring reservoir rock and fluid transport properties. Houston, Texas, USA: Gulf professional publishing.

Williams SJ, Arsenault MA, Buczkowski BJ, Reid JA, Flocks JG, Kulp MA, Penland S, Jenkins CJ. 2006. Surficial sediment character of the Louisiana offshore Continental Shelf region: a GIS Compilation, U.S. Geological Survey Open-File Report 2006-1195. http://pubs.usgs.gov/of/2006/1195/index.htm

Wyllie MRJ, Gregory AR, Gardner GHF. 1958. An experimental investigation of factors affecting elastic wave velocities in porous media. Geophysics. 23(3):459–493. doi: 10.1190/1.1438493.

Wyllie MRJ, Rose WD. 1950. Some theoretical considerations related to the quantitative evaluation of the physical characteristics of reservoir rock from electrical log data. J Petrol Technol. 2(4):105–118. doi: 10.2118/950105-G.

Younes AI, Engelder T, Bosworth W. 1998. Fracture distribution in faulted basement blocks: gulf of Suez, Egypt. In: Coward MP, Daltaban TS, Johnson H, editors. Structural geology in reservoir characterization. Vol. 127. London: Geological Society; p. 167–190.

Younes AI, McClay K. 2002. Development of accommodation zones in the Gulf of Suez-Red Sea rift. Egypt – American Association Of Petroleum Geologists, Bulletin. 86:1003–1026. doi: 10.1306/61EEDC10-173E-11D7-8645000102C1865D.

Zahran ME, 1986. Geology of October Field: Proceedings 8th Exploration Seminar, EGPC, Cairo, v. 1, p. 35–52.